ChemElectroChem

Research Article
doi.org/10.1002/celc.202400309

Chemistry Europe
European Chemical Societies Publishing

www.chemelectrochem.org

Charge Redistribution in $Nise_2/Mos_2$ n–n Heterojunction towards the Photoelectrocatalytic Degradation of Ciprofloxacin

Tunde L. Yusuf,*[a] Olalekan C. Olatunde,[b] Daniel Masekela,[c] Kwena D. Modibane,[c] Damian C. Onwudiwe,[b] and Seshibe Makgato[a]

This study reports the photoelectrocatalytic (PEC) activity of a n–n heterojunction comprising MoS_2 and $NiSe_2$. The synthesis of the composite was achieved through a facile solvothermal method, yielding an exfoliated MoS_2 layered sheet loaded with $NiSe_2$ nanoparticles. Under visible light radiation and an external electric field, the obtained composite $NiSe_2/MoS_2$ exhibited enhanced catalytic activity for ciprofloxacin (CIP) degradation. The $NiSe_2/MoS_2$ heterojunction achieved about 78% degradation efficiency with a first-order kinetic rate of 0.0111 min^{-1}, compared to 38% efficiency and a first-order kinetic rate of 0.0044 min^{-1} observed for MoS_2. The $NiSe_2/MoS_2$ heterojunction was more advantageous due to the synergy of charge carrier induction by visible light radiation and improved charge carrier separation induced by the external electric field. The formation of n–n heterojunction at the interface of the two materials resulted in charge redistribution in the materials, with a simultaneous realignment of the band structure to achieve Fermi energy equilibration. The primary reactive species responsible for CIP degradation was identified as the photo-induced h^+. Furthermore, the catalyst exhibited high stability and reusability, with no significant reduction in activity observed after five experimental cycles. This study reveals the potential of exploring the synergy between the photocatalytic and electrocatalytic processes in removing harmful pharmaceutical compounds from water.

Introduction

The pollution of aquatic systems by pharmaceutical substances has become a significant issue in environmental sustainability and public health.[1] Among these pollutants, ciprofloxacin, a widely used antibiotic, poses significant challenges due to its persistence and potential adverse effects on aquatic ecosystems and human health.[2] To address this issue, advanced oxidation processes (AOPs) have garnered attention for their effectiveness in degrading pharmaceutical compounds.[3] Among AOPs, photoelectrocatalysis (PEC) stands out as a promising technique that combines the advantages of photocatalysis and electrocatalysis, offering enhanced pollutant degradation under visible light irradiation and efficient charge separation.[4]

An essential requirement for a PEC process is the development of a photoanode with high efficiency in trapping light energy for the generation and transmission of charge carriers for the degradation process.[5] As a characteristic 2D layered material, MoS_2 has been extensively applied in optoelectronic devices and semiconductor photocatalysis because of its high charge carrier mobility and excellent optical absorption characteristics.[6] However, rapid photogenerated charge carrier recombination, limited active sites, and laborious catalyst separation and recycling hinder its practical application.[7] A significant challenge with MoS_2 is that the active sites are at the edge due to the S–Mo–S coordination of its crystals, forming unsaturated Mo and S atoms only at the edge.[8] Therefore, several techniques have been explored to improve the catalytic activity of MoS_2, the most explored being the formation of heterostructure with other semiconductor materials such as MoS_2/C_3N_4,[9] MoS_2-Bi_2WO_6,[10] $ZnIn_2S_4/MoS_2$[11] and TiO_2-MoS_2.[12] The layered structure of MoS_2 makes it suitable for the formation of heterostructure, and its properties can also be significantly altered by varying the thickness of the material.[13] To mitigate the challenge of rapid charge carrier recombination, which is the most significant limitation of MoS_2 in its application as a photoanode, three different heterojunction schemes have been identified: type II, Z-scheme, and S-scheme heterojunction. The inherent limitations of type II and Z-scheme heterojunctions, such as the weakening of charge carrier potentials and the hampering of the charge transition process by undesired side redox reaction, restrict their potential in enhancing charge carrier separation in semiconductor heterojunctions.[14]

[a] *Dr. T. L. Yusuf, S. Makgato*
Department of Chemical Engineering, College of Science, Engineering and Technology, University of South Africa (UNISA), Florida Campus, 1710, Johannesburg, South Africa
E-mail: yusuftl@unisa.ac.za

[b] *O. C. Olatunde, D. C. Onwudiwe*
Department of Chemistry, School of Physical and Chemical Sciences, Faculty of Natural and Agricultural Sciences, North-West University, Mafikeng Campus, Private Bag X2046, Mmabatho 2735, South Africa

[c] *D. Masekela, K. D. Modibane*
Department of Chemistry, University of Limpopo, Sovenga, Polokwane, 0727, South Africa

The excellent electronic properties of $NiSe_2$ have attracted significant attention in several applications, such as dye-sensitized solar cells, hydrogen production, and sodium-ion batteries, because of its high-power conversion efficiency, low overpotential, and high discharge capacity.[15] Given the electronic properties and the potential of $NiSe_2$, it could be a suitable co-catalyst for creating an n–n-type heterojunction with improved activity for PEC.

This study reports the PEC performance of $NiSe_2/MoS_2$ heterojunction. The n–n-type heterojunction took advantage of improved charge carrier separation and transport, and the PEC process's external potential in enhancing the material's PEC performance. The insights from this study highlight the benefits of heterostructure engineering for developing functional materials aimed at environmental remediation. Furthermore, the potential application of this material in photoelectrochemical (PEC) technology for water treatment is demonstrated, addressing the challenges posed by pharmaceutical contaminants like ciprofloxacin in aquatic environments.

Results and Discussion

Structure and Morphology

The $NiSe_2$ was prepared by a facile solvothermal synthesis, while the $NiSe_2/MoS_2$ composite was prepared by introducing MoS_2 into the solvothermal process. The crystal structure and morphology of the MoS_2 and $NiSe_2/MoS_2$ were studied by X-ray diffraction and transmission electron microscopy (TEM), as shown in Figure 1. The XRD pattern of MoS_2(Figure 1a) showed a pattern characteristic of hexagonal MoS_2, with *P63/mmc* space group in reference to the JCPDS card no. 37–1492.[16] The high intensity of the peak at $2\theta = 14.3°$, which corresponds to the (002) phase of MoS_2, shows the high thickness of the MoS_2 and suggests a multilayered MoS_2 sheet. The peaks associated with the $NiSe_2$ could not be seen due to the low concentration. The XRD spectra of $NiSe_2/MoS_2$ were similar to that of MoS_2; however, the weakening of the 002 phase peak suggests the exfoliation of the MoS_2 into few-layered MoS_2 due to the incorporation of $NiSe_2$ onto the MoS_2 sheet.[16b] The SEM images of MoS_2 and $NiSe_2/MoS_2$ (Figure 1b&c) show the morphological difference between MoS_2 and $NiSe_2/MoS_2$. The multilayered nature of MoS_2 and the partial exfoliation of MoS_2 in $NiSe_2/MoS_2$ can be observed. This exfoliation could be attributed to the solvothermal treatment the MoS_2 sheet was subjected to during the heterojunction formation. The exfoliation of MoS_2 has been reported to play a significant role in its effectiveness as a photocatalytic material.[17] The TEM images of MoS_2 and $NiSe_2/MoS_2$ (Figure 1d&e) support the SEM images' observation. The exfoliation of MoS_2 in $NiSe_2/MoS_2$ could be seen in the TEM image, while the deposition of $NiSe_2$ nanoparticles on the exfoliated sheets could be vividly observed.

XPS analysis was carried out to investigate the chemical composition and valence state of the samples. The overall survey spectrum of MoS_2 and $NiSe_2/MoS_2$ (Figure 2a&b) indicates the existence of Mo, S, Ni, and Se elements. The high-resolution XPS spectra of Mo 3d, S 2p, Ni 2p and Se 3d in MoS_2 and $NiSe_2/MoS_2$ were also compared. The spectra of MoS_2 (Figure 2c) exhibited two prominent peaks at 229.23 and 232.5 eV, which are due to the Mo^{4+} $3d_{5/2}$ and Mo^{4+} $3d_{3/2}$ components of MoS_2. A peak observed at 226.5 eV is attributed to the S 2 s of MoS_2. The binding energy region of Mo 3d and S 2p shows that the MoS_2 possesses a robust trigonal prismatic configuration.[18] In the spectra of $NiSe_2/MoS_2$, the doublet Mo^{4+} and S, 2 s peaks showed a slight shift to higher binding energy. The Mo^{4+} $3d_{5/2}$ and Mo^{4+} $3d_{3/2}$ peaks shifted to 236.34 and 233.16 eV, respectively. This shift suggests a flow of electron from MoS_2 to $NiSe_2$ after the formation of the $NiSe_2/MoS_2$ heterojunction.[19] However, a small new peak located at

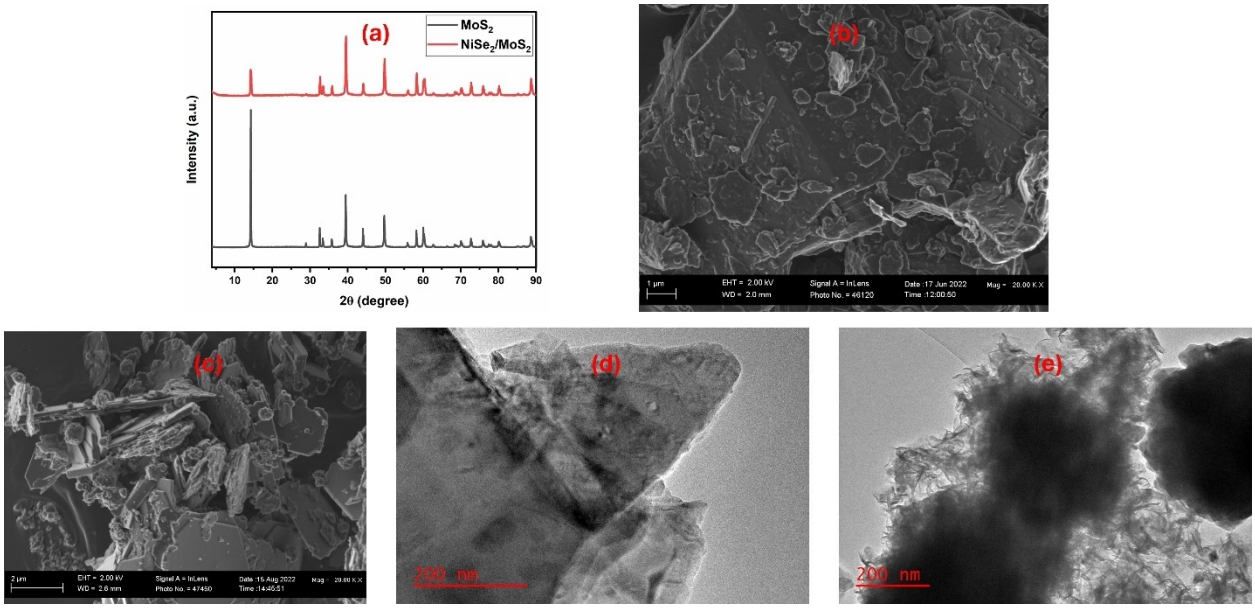

Figure 1. (a) XRD spectra of MoS_2 and $NiSe_2/MoS_2$, (b & c) SEM images of MoS_2 and $NiSe_2/MoS_2$ and (d & e) TEM mages of MoS_2 and $NiSe_2/MoS_2$.

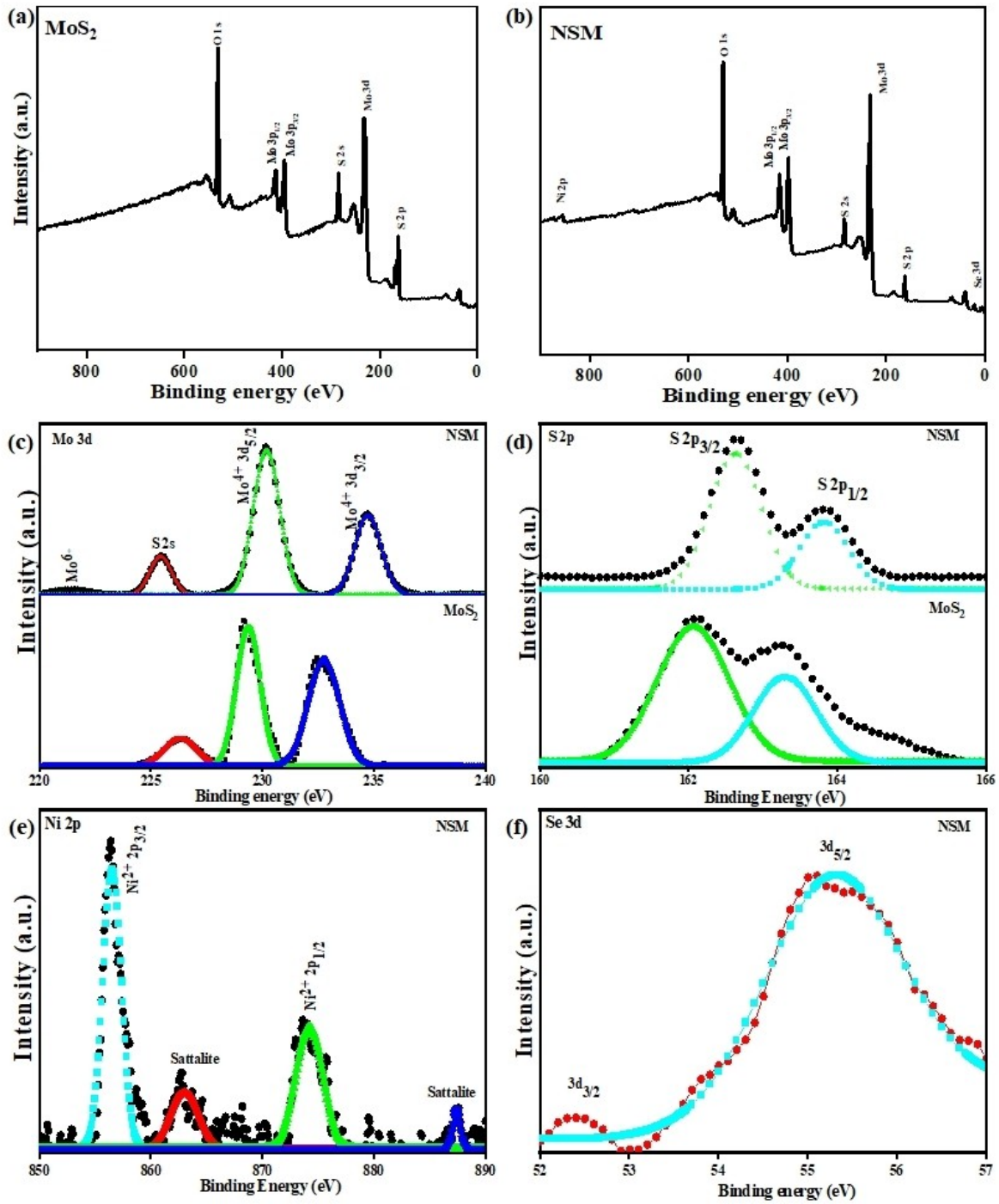

Figure 2. XPS spectra of MoS_2 and $NiSe_2/MoS_2$ (a&b) Overall survey (c) High-resolution spectra for Mo 3d (d) High-resolution spectra for S 2p, (e) High-resolution spectra for Ni 2p and (f) High-resolution spectra for Se 3d.

236.1 eV ascribed to Mo^{6+} was observed, signifying a slight oxidation of the Mo edges in $NiSe_2/MoS_2$ from the Mo^{4+} to the Mo^{6+} state during the hydrothermal synthesis process. This oxidation can modify the electronic properties and produce more active sites for high catalytic activity for the photocatalytic degradation of pollutants.[20] The S 2p spectra for MoS_2 and $NiSe_2/MoS_2$ (Figure 2d) show the S^{2-} doublet at 162.0 and 163.3 eV and 162.7 and 163.8 eV. The shift to higher binding energy confirms the observation in the Mo 3d spectra. The Ni 2p spectra of $NiSe_2/MoS_2$ (Figure 2e) show four peaks. The peaks at 856.4 and 873.8 eV are attributed to the Ni $2p_{3/2}$ and Ni $2p_{1/2}$ states of Ni^{2+}, while the satellite peaks are observed at 862.8 and 879.7 eV.[21] The Se 3d spectra (Figure 2f) exhibited a peak at 55.7 eV, which is attributed to the Se^{2-} anion of $NiSe_2$.[22]

Photo(electro)chemical Characterisation

The modulation of charge carrier dynamics constitutes a pivotal determinant in governing the photocatalytic efficacy of a photocatalytic material. Essential charge carrier attributes, including recombination rate, lifetime, and diffusion length, assume paramount significance in the systematic design of nanostructured photocatalysts.[23] The charge carrier properties of MoS_2 and $NiSe_2/MoS_2$ were systematically explored using electrochemical impedance spectroscopy (EIS) and current density measurements. Analysis of the EIS spectra unveiled discernible semi-circular arcs, providing valuable insights into the charge carrier transport dynamics and the processes governing the separation and transfer resistance of photo-generated carriers. Figure 3(a) depicts the EIS curve obtained for the MoS_2 and $NiSe_2/MoS_2$ electrodes, providing insights into the charge transfer mechanisms and charge carrier recombination dynamics inherent to the materials. The observed decrease in the semi-circular arc diameter within the EIS plot signifies a reduction in the charge-transfer resistance occurring at the interface between the electrode and electrolyte.[24] The EIS curve shows a significant decrease in the semi-circular arc of $NiSe_2/MoS_2$ (21.3 Ω), compared to MoS_2(71.3 Ω) by a factor of 3.5. On this basis, the result indicates that $NiSe_2/MoS_2$ has a low charge-transfer resistance compared to MoS_2, which signifies effective separation of photoinduced charge carriers across the $NiSe_2/MoS_2$ surface due to the introduction of $NiSe_2$. With the low charge transfer resistance, the composite demonstrates an ability to hinder the recombination rate of charge carriers, thereby making them more accessible to participate in PEC activity.[25] In addition, the improved charge separation and transfer efficiency are key factors in enhancing the photocurrent density of the $NiSe_2/MoS_2$ materials. To investigate this, the photocurrent density of MoS_2 and $NiSe_2/MoS_2$ was studied by plotting the current density (I) against potential (V) under illumination and the dark, as shown in Figure 3(b). The current density plot showed that $NiSe_2/MoS_2$ had a higher current density under illumination and in the dark than MoS_2. The current density of $NiSe_2/MoS_2$ was almost two times higher than that of MoS_2, showing the importance of $NiSe_2$, in improving, the charge carrier property of MoS_2 sheet. Furthermore, the transient photocurrent response spectra of MoS_2 and $NiSe_2/MoS_2$under the intermittent illumination of visible light (Figure 3c) shows that $NiSe_2/MoS_2$ had the highest photocurrent

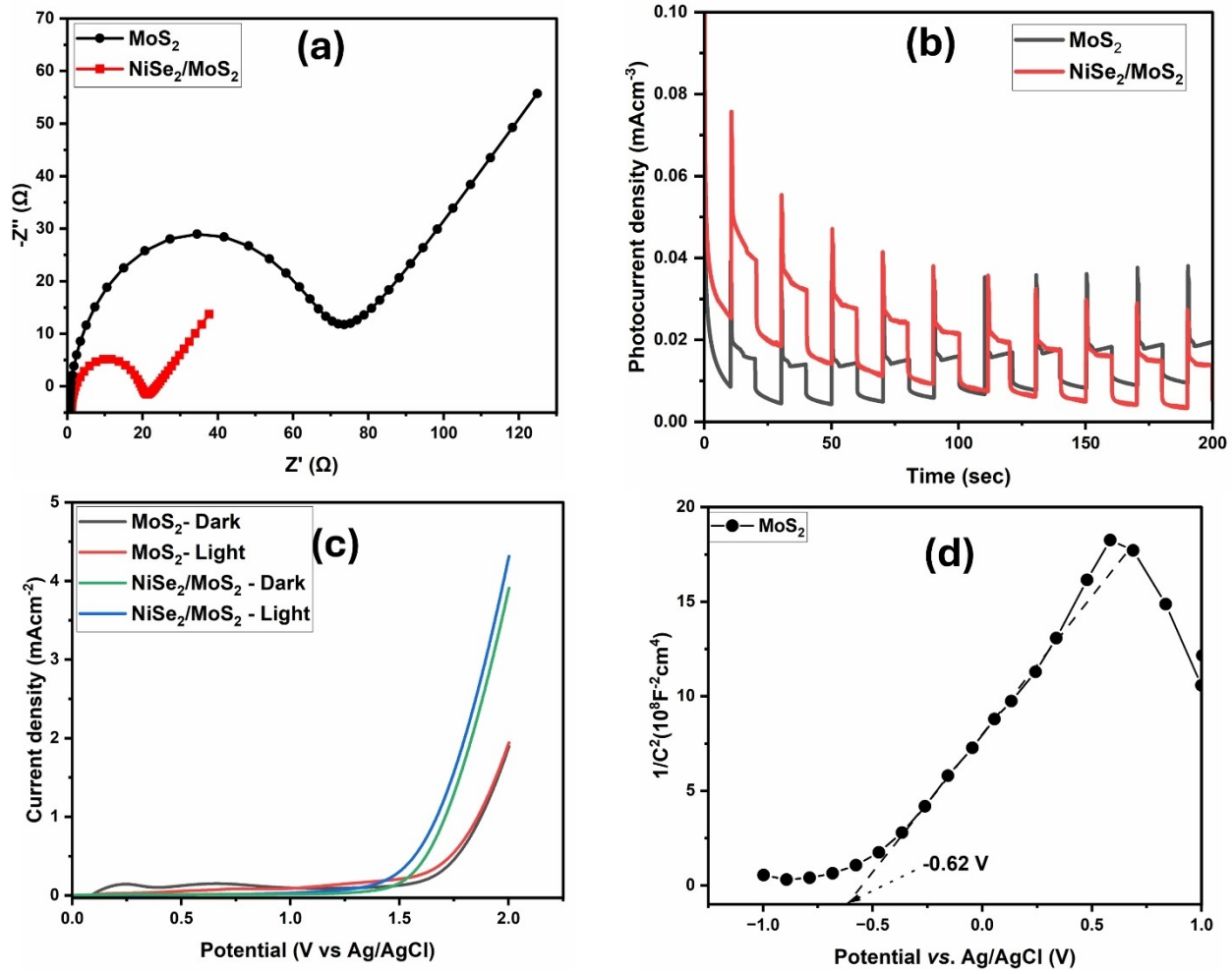

Figure 3. (a) EIS spectra of MoS_2 and $NiSe_2/MoS_2$, (b) photocurrent density of MoS_2 and $NiSe_2/MoS_2$, (c) current density of MoS_2 and $NiSe_2/MoS_2$ in the dark and under illumination and (d) Mott-Schottky plot for MoS_2.

response, indicating that the presence of $NiSe_2$ promoted charge carrier separation and visible-light response ability.[26] A spike in the photocurrent response occurred when the light was switched on, inferring the charge separation between the electrolyte and samples. This instantaneous response positively correlates with efficient electron-hole separation, contributing to improved photocatalytic activity.[27] Both samples displayed a decreasing photocurrent response with time, which could be attributed to hole accumulation.[28] Without illumination, electron transitions from the semiconductor through the FTO and hole migration in the electrolyte led to a rapid photocurrent loss. Similarly, charge carrier recombination in the semiconductor could also account for the photocurrent loss.[29] These results demonstrate $NiSe_2/MoS_2$ superiority over the pristine MoS_2 regarding charge carrier migration and separation.

In Figure 3d, the valence band and conduction band positions of MoS_2 and $NiSe_2/MoS_2$ were evaluated through the Mott-Schottky (MS) plot. The E-C^{-2} plot for the samples showed a positive plot, which suggests n-type semiconductivity.[30] The flat band potential obtained from the Mott-Schottky plot for MoS_2 was −0.62 eV, and by employing the Nernst equation: $E_{NHE} = E_{Ag/AgCl} + 0.197$, the E_{fb} of MoS_2 is calculated to be −0.42 eV vs NHE, respectively. Generally, n-type semiconductors have conduction bands that are about 0.1–0.2 V, more negative than the E_{fb}.[31] Therefore, the E_{CB} values for MoS_2 were evaluated to be −0.32 eV vs. NHE. Furthermore, employing the $E_{cb} = E_{vb} - E_g$ relation, the valence band (E_{vb}) for MoS_2 was estimated to be 2.04 eV vs NHE.

The optical absorption and electronic properties of pristine MoS_2 and $NiSe_2/MoS_2$ (Figure 4a) were studied by UV-Vis spectroscopy. The pristine MoS_2 showed broad absorption in the visible region with an absorption edge at around 450 nm. The incorporation of $NiSe_2$ with MoS_2 in $NiSe_2/MoS_2$ was observed to enhance the visible light absorption property of $NiSe_2/MoS_2$. The absorption edge in $NiSe_2/MoS_2$ shifted to a longer wavelength of ~500 nm, which indicates interfacial charge transfer between MoS_2 and $NiSe_2$. In addition, the exfoliation of the MoS_2 into few-layered structures could also contribute to the enhanced absorption due to indirect to direct band gap crossover in MoS_2 with few layers.[16a,32] The Tauc plot was employed in calculating the band gap energy of MoS_2 and

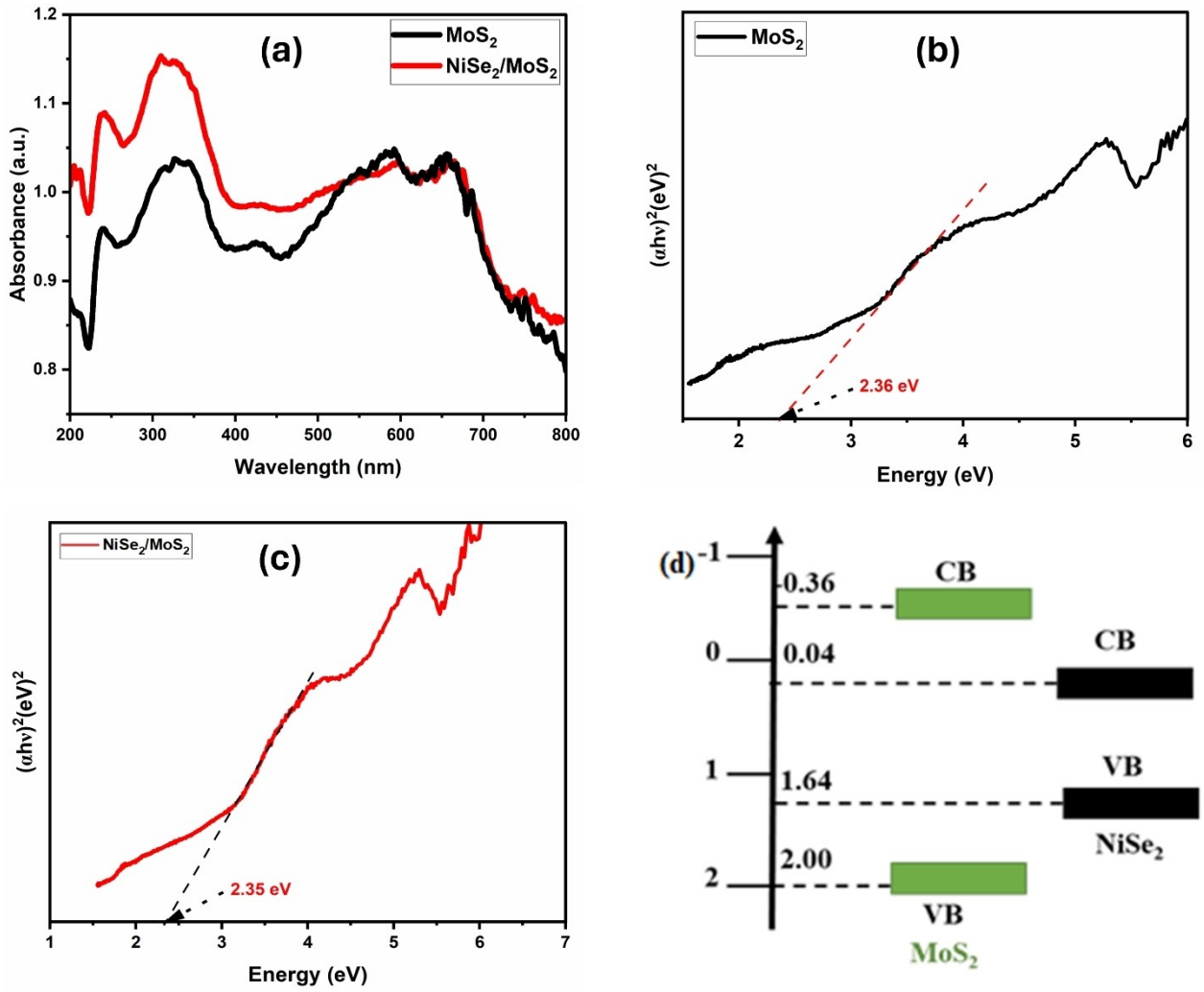

Figure 4. (a) UV-Vis spectra of MoS_2 and $NiSe_2/MoS_2$, (b&c) Tauc plots for MoS_2 and $NiSe_2/MoS_2$and (d) Band alignment for MoS_2 and $NiSe_2$.

$NiSe_2/MoS_2$ (Figure 4b&c). The calculated band gap energy for MoS_2 and $NiSe_2/MoS_2$ are 2.36 eV and 2.35 eV, respectively.

The energies of the E_{CB} and the E_{VB} of the samples can also be theoretically derived from the band gap energy E_g, the energy of the free electrons on the hydrogen scale (E_e 4.5 eV) and the Mulliken electronegativity of the semiconductors *X* (5.34 eV and 5.32 eV for NiSe and MoS_2, respectively)[33] according to Eq. 1 & 2:

$$E_{vb} = X - E^e + 0.5E_g \quad (1)$$

$$E_{cb} = E_{vb} - E_g \quad (2)$$

From the calculation, the E_{CB} potential of MoS_2 (−0.36 eV) is higher compared to that of $NiSe_2$(0.04 eV), while the E_{VB} of MoS_2(2.00 eV) is lower compared to that of $NiSe_2$ (1.6 e eV). This confirms the nesting of the $NiSe_2$ band gap by that of MoS_2, as shown in Figure 4d.

Degradation studies

The photoelectrocatalytic activities of MoS_2 and $NiSe_2/MoS_2$ photoanodes were investigated for the degradation of CIP for 120 mins. The efficiency of the process was monitored by measuring the absorbance of the aliquots taken from the solution at regular intervals. For pristine MoS_2, the photoanode achieved approximately 35% (0.0047 min^{-1}), while a significantly enhanced 78% (0.0111 min^{-1}) degradation efficiency was achieved by $NiSe_2/MoS_2$ photoanode under the same condition (Figure 5a&b). This shows the significant improvement in PEC activity induced by heterojunction formation between MoS_2 and $NiSe_2$. To determine the synergy between photocatalysis and electrocatalysis, the degradation efficiency of CIP was evaluated for the individual process (Figure 5c&d). The degradation efficiency was 20% (0.00146 min^{-1}) and 57% (0.00408 min^{-1}) for photocatalysis and electrocatalysis, respectively. To estimate this synergy between the two processes, the synergistic effect (S), which is the ratio of the rates observed in the hybrid process to the sum of the rates of the individual

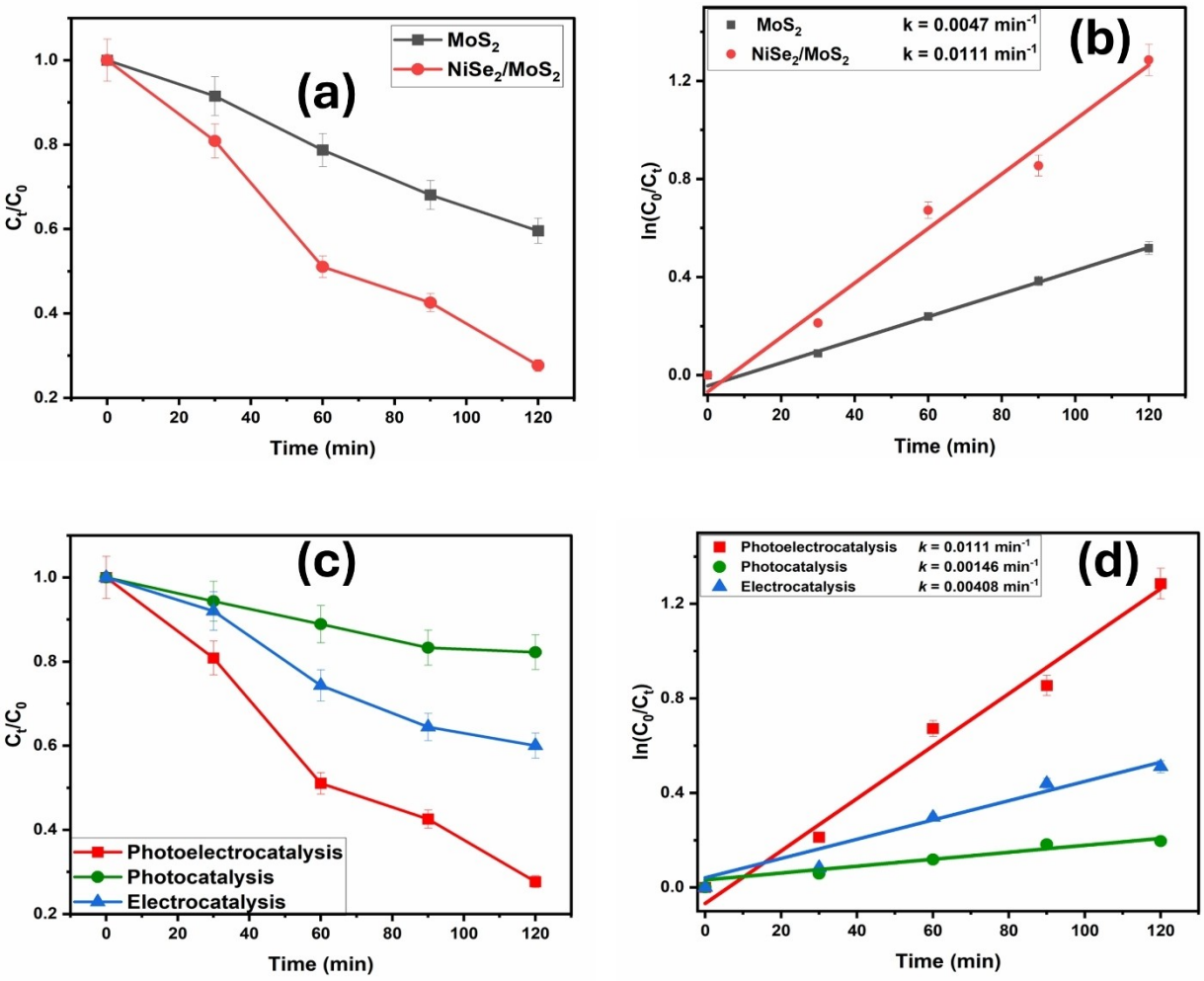

Figure 5. (a) Photoelectrocatalytic degradation profile of CIP by MoS_2 and $NiSe_2/MoS_2$ (b) First order kinetic plot for CIP degradation by MoS_2 and $NiSe_2/MoS_2$ (c) Degradation profile of CIP by $NiSe_2/MoS_2$ in photo electrocatalytic, photocatalytic and electrocatalytic processes and (d) First order kinetic plot of photo electrocatalytic, photocatalytic and electrocatalytic degradation of CIP.

process, was evaluated.[34] The value of S for the PEC process using $NiSe_2/MoS_2$ photoanode was 2.00, showing a strong synergy between the two processes. Furthermore, a comparison of CIP degradation by $NiSe_2/MoS_2$ photoanode with other MoS_2-based materials (Table 1) showed its activity is on par with them.

Five catalytic treatment cycles were evaluated for CIP degradation to investigate the $NiSe_2/MoS_2$ photoanode's stability. The $NiSe_2/MoS_2$ showed strong stability with only a slight reduction after five cycles (Figure 6a). Furthermore, the roles of radical species: superoxides($O_2^{\bullet-}$), holes (h^+) and hydroxyl ($^{\cdot}OH$) radical were investigated by introducing radical scavenging species, triethanol amine (TEA), ethylene diamine (EDTA-Na) and isopropanol (IPA) into the system. Figure 6b shows a reduction in the efficiency of the PEC process by 7%, 11% and 59% on introducing IPA, TEA and EDTA, respectively. This shows that h^+ played the most significant role in the catalytic activity of $NiSe_2/MoS_2$, while $O_2^{\bullet-}$ and $^{\cdot}OH$ only played minor roles.

Photoelectrocatalytic Degradation Mechanism of CIP by $NiSe_2/MoS_2$

The band alignment scheme presented earlier shows the straddling of the band structure of $NiSe_2$ within that of MoS_2, which seems unfavourable for enhanced catalytic activity prior to the formation of the heterostructure. However, with the formation of the n–n heterojunction, a charge redistribution of $NiSe_2$ and MoS_2 occurs at the materials' interface. The flow of electrons is usually from the material with the higher Fermi level (E_F) to the one with the lower Fermi level. It continues until there is an equilibration of the E_F levels. The Fermi energy level of MoS_2 (4.57 eV)[39] and $NiSe_2$ (4.52 eV)[40] implies that the flow of electron is from MoS_2 to $NiSe_2$, which leads to the downward movement of the energy band positions of MoS_2 towards positive potential and those of $NiSe_2$ move up to more negative potential.[41] Furthermore, photoinduced charge carriers are generated by the promotion of electrons from the valence band of both MoS_2 and $NiSe_2$ into the valence band. Due to the n–n heterojunction at the interface, the built-in electric field drives the transfer of excited electrons from the CB of MoS_2 and combines with the holes in the VB of $NiSe_2$. Under the applied external potential, the electrons on the CB of $NiSe_2$ migrate to the counter electrode, with the holes on the VB of MoS_2 available for the degradation of CIP. This proposed charge transfer mechanism in $NiSe_2/MoS_2$heterojunction (Figure 7) agrees with the radical scavenging experiments and accounts for the high synergy between the photocatalytic and electrocatalytic processes.

Conclusions

The $NiSe_2/MoS_2$ heterostructure has been successfully fabricated by a facile solvothermal method and confirmed by characterization techniques such as XRD, SEM, TEM and XPS analysis. The study comprehensively explored the photoelectrocatalytic (PEC) performance of the $NiSe_2/MoS_2$ heterojunction in ciprofloxacin

Table 1. *Comparison of CIP degradation by previously reported MoS2-based heterojunction photocatalyst.*

Catalysts	Process	Catalyst Dosage	CIP	Degradation	Rate constant	Ref.
$Fe_3CN@MoS_2$-4	Photo-assisted peroxymonosulfate	30 mg	10 mg/L, 100 mL, 140 min.	83%	0.0052 min^{-1}	[35]
MoS_2/ZnO	Photocatalysis	50 mg	0.05 M, 100 mL, 120 min	89%	0.014 min^{-1}	[36]
$Mos_2/CoTiO_3$	Photocatalysis	50 mg	20 ppm, 50 mL, 90 min	82%	0.0279 min^{-1}	[37]
$MoS_2/PbBiO_2I$	Photocatalysis	30 mg	10 mg/L, 100 mL, 120 min	84%	–	[38]
$MoS_2/NiSe_2$	Photoelectrocatalysis	50 mg	5 mg/L, 100 mL, 120 min	78%	0.0111	This study

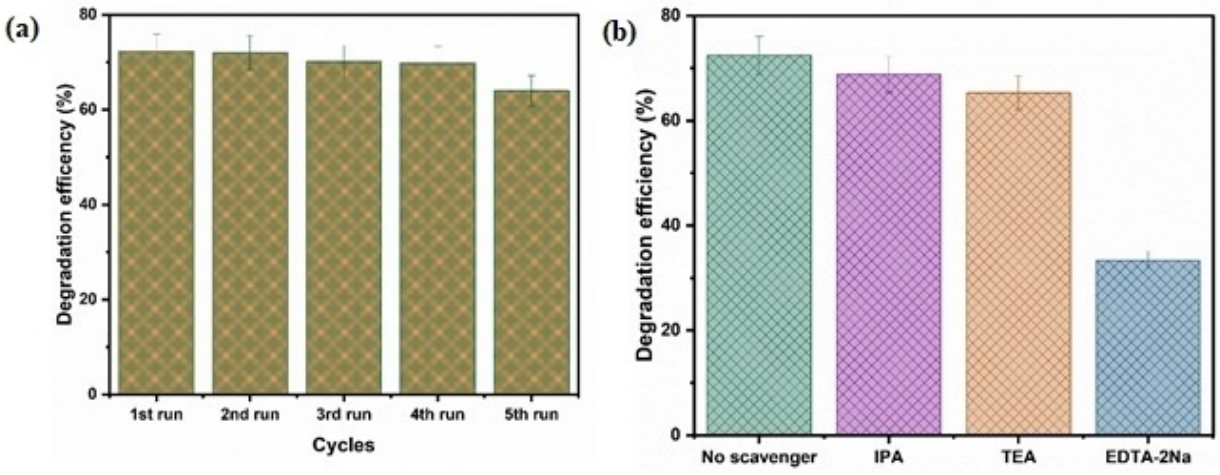

Figure 6. (a) 5-cycle stability test for $NiSe_2/MoS_2$ and (b) Radical scavenging experiment for PEC degradation of CIP.

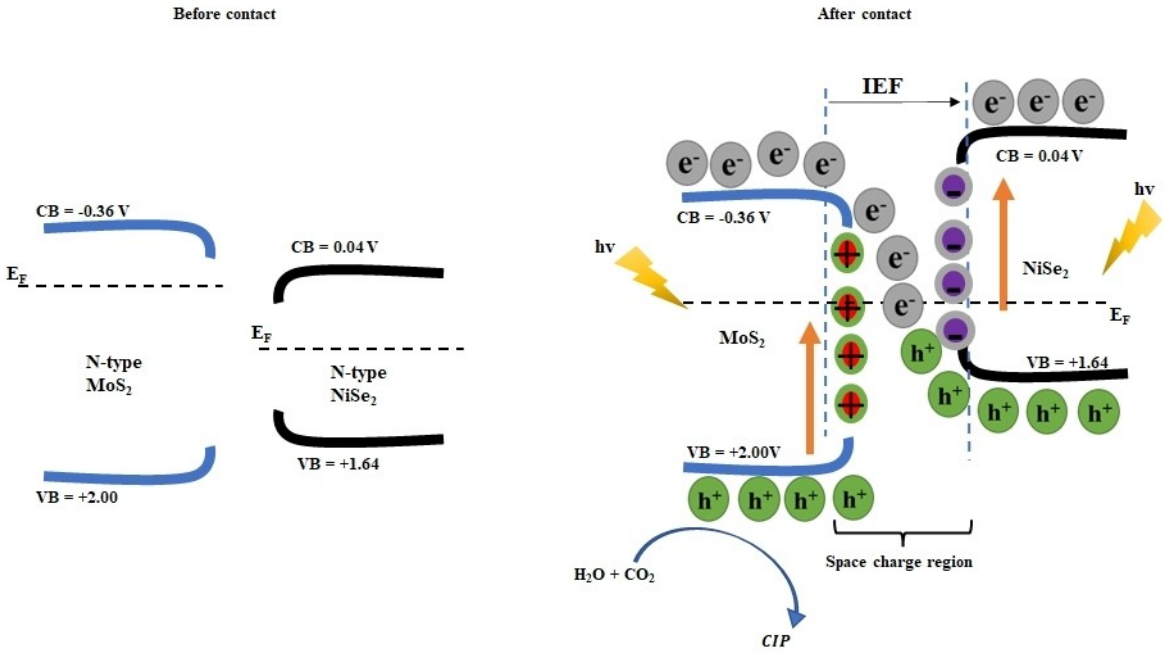

Figure 7. Proposed mechanism for the PEC degradation of CIP.

(CIP) degradation, a prevalent antibiotic contaminant. Our findings demonstrate that the $NiSe_2/MoS_2$ heterojunction significantly enhances PEC activity, achieving a degradation efficiency of approximately 78%, notably surpassing the 38% efficiency exhibited by MoS_2 alone. This improvement is largely attributed to the effective charge redistribution and realignment of band structures at the n–n interface, facilitating better charge carrier separation and utilization under the influence of visible light and an external electric field. Additionally, the stability and reusability tests of the $NiSe_2/MoS_2$ composite indicate no substantial loss in activity over five cycles, underscoring its potential for long-term application in water treatment processes. By further mechanistic investigation, parameter optimization, and pilot scale, we can further harness the potential of n–n heterojunctions like $NiSe_2/MoS_2$ in environmental remediation, particularly in the efficient and sustainable removal of hazardous pharmaceuticals from wastewater.

Experimental

Materials

Nickel chloride hexahydrate ($NiCl_2.6H_2O$), sodium selenite (Na_2SeO_3), ethylene glycol (EG), Molybdenum disulfide (MoS_2) ciprofloxacin (CIP), acrylamide, Polyvinylidene fluoride, *N*-methyl-2-pyrrolidone, sodium sulfate (Na_2SO_4), disodium salt of ethylenediaminetetracetate (Na_2EDTA), tert-butanol (t-BuOH), acrylamide, potassium tetraoxomanganate (VII) ($KMnO_4$), potassium hexacyanoferrate (II) ($K_4Fe(CN)_6$) and potassium hexacyanoferrate (III) ($K_3Fe(CN)_6$). No further purification was carried out on all the chemicals obtained from Sigma-Aldrich (South Africa).

Synthesis of $NiSe_2/MoS_2$

The $NiSe_2/MoS_2$ synthesis was achieved through the in-situ deposition of $NiSe_2$ onto MoS_2. Initially, 1.0 mmol of MoS_2 was dispersed in ethylene glycol and subjected to ultrasonication for 1 hour. Afterward, a solution containing $NiCl_2.6H_2O$ (0.025 mmol) and Na_2SeO_3 (0.05 mmol) was added and sonicated for 30 minutes. The mixture was then transferred into a 100 mL Teflon-lined autoclave and placed in a muffle furnace at 180 °C for 24 hours. Subsequently, the solution was allowed to cool naturally, and the residue was collected, washed three times with ethanol and water, and dried in an oven at 70 °C for 12 hours to obtain $NiSe_2/MoS_2$.

Characterization

A Rigaku Ultima IV X-ray diffractometer (XRD) sourced from Japan was used to discern the crystalline phases within the composite and pristine samples. The X-ray radiation source employed was Cu Kα (λ = 1.5406 Å), enhanced with a K-β filter, operating at 30 mA and 40 kV. To examine the shapes and constituent elements of the samples, a Field Emission Scanning Electron Microscope (FE-SEM), specifically the Zeiss Crossbeam 540 model from the United Kingdom, was employed, coupled with Energy Dispersive X-ray Spectroscopy (EDS). High-resolution images were captured using a JEM-2100 transmission electron microscope (TEM) from Japan. Electronic absorption spectra were collected using a Cary 60 UV-vis spectrometer manufactured by Agilent Technologies in Malaysia. Electrochemical impedance spectroscopy, Mott Schottky analysis, and photocurrent response measurements were conducted utilising an Autolab Potentiostat workstation (PGSTAT204) from the Netherlands. The photoluminescence spectra were recorded on Shimadzu spectrofluorophotometer RF-6000.

Fabrication of Photoanode

To construct the photoanode, Fluorine-doped tin oxide (FTO) was used as the base for electrode production. The catalysts were applied to the substrate using the drop-casting method. Initially, the FTO glass was cleaned by sonication in acetone for 10 minutes, followed by a rinse with water and drying at 60 °C. For the catalyst dispersion, 100 μL of N-methyl-2-pyrrolidone and 5 mg of polyvinylidene fluoride were combined with 50 mg of each MoS_2 and $NiSe_2/MoS_2$ sample and stirred continuously to form a uniform slurry. The slurry was then carefully spread over the conductive surface of the FTO glass, measuring 1.7 cm by 1.7 cm, to ensure an even layer. After application, the coated glass was dried in an oven at 60 °C for 2 hours.

Photoelectrochemical Study

The PEC (photoelectrochemical) studies utilized a traditional three-electrode cell setup, which included a Pt wire as the counter electrode, an Ag/AgCl (in 3.0 M KCl) as the reference electrode, and the specially designed photoanode serving as the working electrode. Illumination was provided by a 100 W xenon solar lamp. The incident light source and the photoanode were arranged vertically, maintaining a 10 cm distance between them. The electrolyte used for the impedance spectroscopy analysis was a solution of 5 mM $[Fe(CN)_6]^{3-}/[Fe(CN)_6]^{4-}$ in 0.1 M KCl, with an applied potential of +0.25 V, conducted without light at frequencies ranging from 100 kHz to 0.1 Hz. The impedance spectroscopy (EIS) data were analyzed using a Randles circuit model. Mott-Schottky measurements were taken in darkness, using an electrolyte solution of 5 mM $[Fe(CN)_6]^{3/4-}$ in 0.1 M KCl. For photocurrent level assessment, a 0.1 M Na_2SO_4 solution was employed. The degradation process of CIP was carried out in a 100 mL quartz glass container.

Degradation of Ciprofloxacin (CIP)

The degradation of CIP was carried out in a quartz glass container with a capacity of 100 mL with a bias potential of 1.2 V. The electrolyte solution consisted of 5 mg/L CIP dissolved in 0.1 M Na_2SO_4. To examine the impact of electrolysis on the degradation process, the experiment was replicated without exposure to light. The degradation progress was monitored by measuring the absorbance of the CIP sample at 30 min intervals using a UV-vis spectrophotometer.

Conflict of Interests

The authors declare no conflict of interest.

Data Availability Statement

The data that support the findings of this study are available from the corresponding author upon reasonable request.

Keywords: photoelectrocatalytic degradation · n–n heterojunction · ciprofloxacin · pharmaceutical

[1] a) A. Kock, H. C. Glanville, A. C. Law, T. Stanton, L. J. Carter, J. C. Taylor, *Sci. Total Environ.* **2023**, *878*, 162939; b) I. Pinto, M. Simões, I. B. Gomes, *Antibiotics* **2022**, *11*, 1700; c) S. Faryad, U. Azhar, M. B. Tahir, W. Ali, M. Arif, M. Sagir, *Chemosphere* **2023**, *320*, 138002.
[2] I. Tantis, L. Bousiakou, G.-A. Karikas, P. Lianos, *Photochem. Photobiol. Sci.* **2015**, *14*, 603–607.
[3] N. Roy, S. A. Alex, N. Chandrasekaran, A. Mukherjee, K. Kannabiran, *J. Environ. Chem. Eng.* **2021**, *9*, 104796.
[4] a) Q. Dang, L. Wang, J. Liu, D. Wang, J. Chai, M. Wu, L. Tang, *J. Water Proc. Eng.* **2023**, *53*, 103609; b) T. L. Yusuf, S. A. Ogundare, F. Opoku, N. Mabuba, *Surfaces and Interfaces* **2023**, *36*, 102534.
[5] a) B. O. Orimolade, O. A. Arotiba, *Sci. Rep.* **2020**, *10*, 5348; b) T. Mohlala, T. L. Yusuf, N. Mabuba, *J. Electroanal. Chem.* **2023**, *947*, 117806.
[6] a) L. Wei, Y. Chen, Y. Lin, H. Wu, R. Yuan, Z. Li, *Appl. Catal. B* **2014**, *144*, 521–527; b) Q. Xiang, J. Yu, M. Jaroniec, *J. Am. Chem. Soc.* **2012**, *134*, 6575–6578; c) X. Jin, X. Fan, J. Tian, R. Cheng, M. Li, L. Zhang, *RSC Adv.* **2016**, *6*, 52611–52619; d) Y. Wang, G. Li, P. Li, J. Hu, Q. Zhao, *Bandaoti Guangdian/Semicond Optoelectron* **2016**, *37*, 461–466; e) O. C. Olatunde, T. L. Yusuf, N. Mabuba, D. C. Onwudiwe, S. Makgato, *J. Water Proc. Eng.* **2024**, *59*, 105074.
[7] Z. Li, X. Meng, Z. Zhang, *Journal of Photochemistry and Photobiology C: Photochemistry Reviews* **2018**, *35*, 39–55.
[8] Y. J. Yuan, H. W. Lu, Z. T. Yu, Z. G. Zou, *ChemSusChem* **2015**, *8*, 4113–4127.
[9] J. Yan, Z. Chen, H. Ji, Z. Liu, X. Wang, Y. Xu, X. She, L. Huang, L. Xu, H. Xu, *Chemistry–A European Journal* **2016**, *22*, 4764–4773.
[10] X. Meng, Z. Li, H. Zeng, J. Chen, Z. Zhang, *Appl. Catal. B* **2017**, *210*, 160–172.
[11] W. Y. Lim, M. Hong, G. W. Ho, *Dalton Trans.* **2016**, *45*, 552–560.
[12] S. Bai, L. Wang, X. Chen, J. Du, Y. Xiong, *Nano Res.* **2015**, *8*, 175–183.
[13] R. Yang, J. Fan, M. Sun, *Frontiers of Physics* **2022**, *17*, 43202.
[14] a) Q. Xu, L. Zhang, B. Cheng, J. Fan, J. Yu, *Chem* **2020**, *6*, 1543–1559; b) T. Teranishi, M. Sakamoto, *J. Phys. Chem. Lett.* **2013**, *4*, 2867–2873; c) K. Maeda, *ACS Catal.* **2013**, *3*, 1486–1503.
[15] a) F. Gong, X. Xu, Z. Li, G. Zhou, Z.-S. Wang, *Chem. Commun.* **2013**, *49*, 1437–1439; b) H. Fan, H. Yu, X. Wu, Y. Zhang, Z. Luo, H. Wang, Y. Guo, S. Madhavi, Q. Yan, *ACS Appl. Mater. Interfaces* **2016**, *8*, 25261–25267; c) H. Zhou, Y. Wang, R. He, F. Yu, J. Sun, F. Wang, Y. Lan, Z. Ren, S. Chen, *Nano Energy* **2016**, *20*, 29–36.
[16] a) S. Nayak, G. Swain, K. Parida, *ACS Appl. Mater. Interfaces* **2019**, *11*, 20923–20942; b) S. Iqbal, Z. Pan, K. Zhou, *Nanoscale* **2017**, *9*, 6638–6642; c) Y. Liu, Y.-X. Yu, W.-D. Zhang, *J. Phys. Chem. C* **2013**, *117*, 12949–12957.
[17] D. Sahoo, B. Kumar, J. Sinha, S. Ghosh, S. Roy, B. Kaviraj, *Sci. Rep.* **2020**, *10*, 12.
[18] B. Li, L. Jiang, X. Li, P. Ran, P. Zuo, A. Wang, L. Qu, Y. Zhao, Z. Cheng, Y. Lu, *Scientific Reports* **2017**, *7*, 11182.
[19] C. Cheng, J. Zhang, B. Zhu, G. Liang, L. Zhang, J. Yu, *Angew. Chem. Int. Ed.* **2023**, *62*, e202218688.
[20] a) Z. Wu, B. Fang, Z. Wang, C. Wang, Z. Liu, F. Liu, W. Wang, A. Alfantazi, D. Wang, D. P. Wilkinson, *ACS Catal.* **2013**, *3*, 2101–2107; b) D. Voiry, M. Salehi, R. Silva, T. Fujita, M. Chen, T. Asefa, V. B. Shenoy, G. Eda, M. Chhowalla, *Nano Lett.* **2013**, *13*, 6222–6227.
[21] a) G. Shombe, M. Khan, C. Zequine, C. Zhao, R. Gupta, N. Revaprasadu, *Scientific Reports* **2020**, *10*, 3260; b) T. Chen, Z. Liu, Z. Liu, X. Tao, H. Fan, L. Guo, *Mater. Lett.* **2019**, *248*, 1–4.
[22] A. T. Swesi, J. Masud, M. Nath, *Energy Environ. Sci.* **2016**, *9*, 1771–1782.
[23] T. J. Miao, J. Tang, *The Journal of Chemical Physics* **2020**, *152*, 194201.
[24] a) S. Nayak, A. C. Pradhan, K. M. Parida, *Inorg. Chem.* **2018**, *57*, 8646–8661; b) S. Nayak, K. M. Parida, *ACS Omega* **2018**, *3*, 7324–7343.
[25] a) J. Choi, P. Sudhagar, J. H. Kim, J. Kwon, J. Kim, C. Terashima, A. Fujishima, T. Song, U. Paik, *Phys. Chem. Chem. Phys.* **2017**, *19*, 4648–4655; b) D. Cao, Y. Wang, M. Qiao, X. Zhao, *J. Catal.* **2018**, *360*, 240–249.
[26] a) H. Liu, T. Yan, Z. Jin, Q. Ma, *New J. Chem.* **2020**, *44*, 14879–14889; b) C. Cheng, J. Shi, F. Du, S. Zong, X. Guan, Y. Zhang, M. Liu, L. Guo, *Catalysis Science, Technology* **2019**, *9*, 7016–7022; c) S. Wang, Y. Wang, S. L. Zhang, S.-Q. Zang, X. W. Lou, *Adv. Mater.* **2019**, *31*, 1903404.
[27] S. Le, T. Jiang, Y. Li, Q. Zhao, Y. Li, W. Fang, M. Gong, *Appl. Catal. B* **2017**, *200*, 601–610.
[28] S. Wang, B. Zhu, M. Liu, L. Zhang, J. Yu, M. Zhou, *Appl. Catal. B* **2019**, *243*, 19–26.
[29] a) F. W. P. Ribeiro, M. F. Gromboni, F. Marken, L. H. Mascaro, *Int. J. Hydrogen Energy* **2016**, *41*, 17380–17389; b) T. Soltani, A. Tayyebi, B.-K. Lee, *Catal. Today* **2020**, *340*, 188–196.
[30] Q. Zhu, B. Qiu, H. Duan, Y. Gong, Z. Qin, B. Shen, M. Xing, J. Zhang, *Appl. Catal. B* **2019**, *259*, 118078.
[31] X. Yue, S. Yi, R. Wang, Z. Zhang, S. Qiu, *Nano Energy* **2018**, *47*, 463–473 .

[32] J. Pető, G. Dobrik, G. Kukucska, P. Vancsó, A. A. Koós, J. Koltai, P. Nemes-Incze, C. Hwang, L. Tapasztó, *NPJ 2D Mater. Appl.* **2019**, *3*, 39.
[33] a) T. L. Yusuf, S. A. Ogundare, F. Opoku, O. A. Arotiba, N. Mabuba, *J. Environ. Chem. Eng.* **2023**, *11*, 110711; b) D. Barpuzary, A. Banik, G. Gogoi, M. Qureshi, *J. Mater. Chem. A* **2015**, *3*, 14378–14388.
[34] C. Pétrier in *31 - The use of power ultrasound for water treatment*, Eds.: J. A. Gallego-Juárez, K. F. Graff), Woodhead Publishing, Oxford, **2015**, pp. 939–972.
[35] X. Li, D. Feng, X. He, D. Qian, B. Nasen, B. Qi, S. Fan, J. Shang, X. Cheng, *Sep. Purif. Technol.* **2022**, *303*, 122219.
[36] Y. M. Hunge, A. A. Yadav, S.-W. Kang, S. Jun Lim, H. Kim, *J. Photochem. Photobiol. A* **2023**, *434*, 114250.
[37] R. Dadigala, R. Bandi, M. Alle, B. R. Gangapuram, V. Guttena, J.-C. Kim, *Chemosphere* **2021**, *281*, 130822.
[38] M. Li, S. Yin, T. Wu, J. Di, M. Ji, B. Wang, Y. Chen, J. Xia, H. Li, *J. Colloid Interface Sci.* **2018**, *517*, 278–287.
[39] C. Kim, I. Moon, D. Lee, M. S. Choi, F. Ahmed, S. Nam, Y. Cho, H.-J. Shin, S. Park, W. Yoo, *ACS Nano* **2017**, *11*, 1588–1596.
[40] X. Wen, Z. Ran, R. Zheng, D. Du, C. Zhao, R. Li, H. Xu, T. Zeng, C. Shu, *J. Alloys Compd.* **2022**, *901*, 163703.
[41] H. Gong, Z. Li, Z. Chen, Q. Liu, M. Song, C. Huang, *ACS Appl. Nano Mater.* **2020**, *3*, 3665–3674.

Manuscript received: April 13, 2024
Revised manuscript received: May 15, 2024
Version of record online: July 25, 2024